Phase Transformations in the CeO$_2$−Sm$_2$O$_3$ System: A Multiscale Powder Diffraction Investigation

Mauro Coduri,[*,†,‡,§] Paolo Masala,[†] Mattia Allieta,[†] Inma Peral,[∥,⊥,#] Michela Brunelli,[○] Carlo Alberto Biffi,[§] and Marco Scavini[†,△]

[†]Dipartimento di Chimica, Università degli Studi di Milano, Via C. Golgi 19, I-20133 Milano, Italy

[‡]ESRF−The European Synchrotron, 71, Avenue des Martyrs, 38043, Grenoble, France

[§]Institute of Condensed Matter Chemistry and Technologies for Energy, Unit of Lecco, National Research Council, CNR ICMATE, Via G. Previati 1/E, 23900 Lecco, Italy

[∥]ALBA-CELLS Synchrotron, Carretera BP 1413, Km. 3.3, E-08290 Cerdanyola, Barcelona, Spain

[⊥]Physics and Materials Science Research Unit, University of Luxembourg, 162a avenue de la Faencerie, L-1511 Luxembourg, Luxembourg

[#]Materials Research and Technology Department, Luxembourg Institute of Science and Technology, 41 rue du Brill, L-4422 Belvaux, Luxembourg

[○]Swiss Norwegian beamlines, SNBL-ESRF, 71, Avenue des Martyrs, Grenoble, France

[△]ISTM-CNR and INSTM Unit, Via C. Golgi 19, I-20133 Milano, Italy

S *Supporting Information*

ABSTRACT: The structure evolution in the CeO$_2$−Sm$_2$O$_3$ system is revisited by combining high resolution synchrotron powder diffraction with pair distribution function (PDF) to inquire about local, mesoscopic, and average structure. The CeO$_2$ fluorite structure undergoes two phase transformations by Sm doping, first to a cubic (C-type) and then to a monoclinic (B-type) phase. Whereas the C to B-phase separation occurs completely and on a long-range scale, no miscibility gap is detected between fluorite and C-type phases. The transformation rather occurs by growth of C-type nanodomains embedded in the fluorite matrix, without any long-range phase separation. A side effect of this mechanism is the ordering of the oxygen vacancies, which is detrimental for the application of doped ceria as an electrolyte in fuel cells. The results are discussed in the framework of other Y and Gd dopants, and the relationship between nanostructuring and the above equilibria is also investigated.
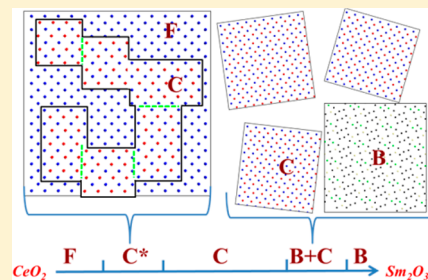
1. INTRODUCTION

Doped ceria materials (Ce$_{1−\mu}$RE$_\mu$O$_{2−y}$, RE = Y and rare earths) are attracting the interest of the scientific community for different reasons. From the technological point of view, the interest comes from their application as electrolytes in solid oxide fuel cells (SOFCs) because of their high ionic conductivity displayed at high and intermediate temperatures.[1] Despite their apparent simplicity, fluorite structures like CeO$_2$ are known to accommodate a high concentration of lattice defects, thus being also a reference system for modeling disorder.[2−4] This aspect is particularly important for doped ceria electrolytes, where doping of ceria with lower valent cations creates oxygen vacancies through which oxygen ions can diffuse via a thermally activated process. As ionic conductivity has inverse dependence on the activation energy needed by oxygen ions to migrate through the lattice,[5] the accurate description of the crystal structure, from the local to the average crystal environment, is of primary importance.

This is particularly true for heavily doped ceria compounds, where the approximation of randomly distributed defects is no

longer valid.[6] In fact, the fluorite structure of cerium oxide is suitable for accommodating defects of different kinds and extents, especially with respect to the nonrandom distribution of oxygen vacancies induced by doping of lower valent cations.[7,8] A number of research papers involving different experimental and computational approaches was aimed at clarifying how defects arrange in doped ceria. Different kinds of aggregations were proposed, either involving few dopant atoms, as suggested by extended X-ray absorption fine structure (EXAFS)[9,10] and NMR,[11] or larger nanodomains tens of nanometers wide, as probed by electron microscopy[12,13] and atomic pair distribution function (PDF).[14,15] This picture was confirmed computationally only recently,[16,17] as the modeling of such big aggregates requires advanced computation strategies.

In the case of Sm doping, to which superior SOFC performance among rare earth dopants is attributed,[18,19] the

Table 1. Details of the Samples Investigated through Synchrotron Radiation and Corresponding Data Analysis Strategy[a]

nominal elemental composition	nominal Sm/(Sm + Ce)	probed Sm/(Sm + Ce)	final annealing temperature (°C)	phases	XRPD analysis	source
CeO_2	0		900	F	Rietveld + PDF	ESRF
$Ce_{0.875}Sm_{0.125}O_{1.938}$	2/16	0.111(3)	900	F	Rietveld + PDF	ESRF
$Ce_{0.750}Sm_{0.250}O_{1.875}$	4/16	0.223(8)	900	F	Rietveld + PDF	ESRF
$Ce_{0.687}Sm_{0.313}O_{1.844}$	5/16	0.286(8)	500	F	Rietveld + PDF	ALBA
			900	F	Rietveld + PDF	ESRF
$Ce_{0.656}Sm_{0.344}O_{1.828}$	5.5/16	0.323(9)	500	F	Rietveld + PDF	ALBA
			900	C*[b]	Rietveld + PDF	ESRF
$Ce_{0.625}Sm_{0.375}O_{1.813}$	6/16	0.351(8)	500	C*[b]	Rietveld + PDF	ALBA
			900	C*[b]	Rietveld + PDF	ESRF
$Ce_{0.594}Sm_{0.406}O_{1.797}$	6.5/16	0.374(7)	900	C*[b]	Rietveld	ESRF
$Ce_{0.562}Sm_{0.438}O_{1.781}$	7/16	0.41(1)	900	C*[b]	Rietveld + PDF	ESRF
$Ce_{0.500}Sm_{0.500}O_{1.750}$	8/16	0.465(9)	900	C	Rietveld + PDF	ESRF
$Ce_{0.438}Sm_{0.562}O_{1.719}$	9/16	0.533(4)	900	C	Rietveld	ESRF
$Ce_{0.375}Sm_{0.625}O_{1.688}$	10/16	0.598(4)	900	C	Rietveld + PDF	ESRF
$Ce_{0.312}Sm_{0.688}O_{1.656}$	11/16	0.662(4)	900	C	Rietveld	ESRF
$Ce_{0.250}Sm_{0.750}O_{1.625}$	12/16	0.715(3)	900	C	Rietveld + PDF	ESRF
$Ce_{0.187}Sm_{0.813}O_{1.594}$	13/16	0.796(2)	900	C	Rietveld	ESRF
$Ce_{0.125}Sm_{0.875}O_{1.563}$	14/16	0.867(3)	900	C + B (6.5(1)%)	Rietveld + PDF	ESRF
$Ce_{0.062}Sm_{0.938}O_{1.531}$	15/16	0.933(3)	900	C + B (19.3(1)%)	Rietveld + PDF	ESRF
			1000	C + B (37.9(1)%)	Rietveld + PDF	ESRF
Sm_2O_3	1		900	B	Rietveld + PDF	ESRF
			700	C	Rietveld + PDF	ESRF

[a]When not explicitly stated, the samples are pure in phase. [b]C-type phase, though characterized by the selective broadening of superstructure peaks only.

conductivity drop is reported at a critical concentration range from μ = 0.15[20] to 0.20[21] and 0.25.[22] Literature studies disagree about the effective solubility limit of Sm into CeO_2. Whereas Mandal et al.[23] observed direct transformation from fluorite to C-type by increasing μ from 0.4 to 0.5, large biphasic regions were observed in refs 24 and 25. A more complex model was proposed by Artini et al.,[26,27] who described through Raman and X-ray powder diffraction (XRPD) the intermediate compositional region with a hybrid structure between those of CeO_2 and Sm_2O_3.

While conventional powder diffraction via the Rietveld method may be insensitive to local orderings, PDF is well-suited to overcome this problem. Recent powder diffraction studies on Gd,[15,28] Y,[14] and on other rare earth dopants (La, Nd, Yb;[29] Pr and Tb[30]), besides those on Bi[31] and Zr,[32] revealed a common complex scheme of defect structure evolution with doping, which also applies under operating conditions.[33] It is based on the clustering of dopant ions and oxygen vacancies to form nanodomains resembling the structure of the dopant oxide. This is of special interest for Sm doping, since Sm_2O_3 crystallizes not only as cubic C-type, like other sesquioxides, but also in a monoclinic form.[34]

Since the formation of dopant-rich aggregates is often suggested to be the main driving force for modifications of transport properties,[5] here we use for the first time the same combined PDF and Rietveld approach to investigate the structure evolution over Sm doping, extending the investigation to the full CeO_2–Sm_2O_3 system and placing special emphasis on the transformation of doped ceria from fluorite to C-type and from C- to B-type phases.

Since the former has direct impact on the application of the material as an electrolyte in SOFCs, here it is further investigated on samples produced with a crystallite size comparable to that of the observed nanodomains.

2. EXPERIMENTAL SECTION

2.1. Synthesis. $Ce_{1-\mu}Sm_\mu O_{2-\mu/2}$ samples with different μ Sm concentration were prepared with the *Pechini* sol−gel method.[35] The as prepared gel was first burned for 3 h at 500 °C in an ashing furnace; then, the furnace was turned off and the samples were cooled inside it. Aliquots of the samples were then fired at 900 °C for 72 h in air and cooled inside the oven. CeO_2 (>99%) was purchased by Fluka. Additional firing procedures for samples in the $0.750 \leq \mu \leq 1$ range are described in the Supporting Information (SI). The powders obtained just after burning at 500 °C will be referred to as "nano", those sintered at 900 °C, as "sint". The list of the samples investigated, here labeled as the element symbol followed by the μ concentration value, is given in Table 1.

2.2. Data Collection. XRPD patterns on the sint series were collected at 90 K at the ID31 high resolution powder diffraction (HRPD) beamline of the ESRF with λ = 0.35413 Å in the $0 < 2\theta < 120°$ range, employing data for the Fourier transformation up to $Q_{max} \sim 28$ Å^{-1}, where $Q = 4\pi \sin \theta/\lambda$ is the transfer momentum. The powdered samples were packed into 0.7 mm kapton capillaries to optimize transmission. The wavelength was chosen to guarantee a proper balance between Q_{max} available, incident photon flux, and limited absorption factor. All samples were spun during acquisition to enhance powder averaging. The conventional high resolution setup of ID31 was employed.[36] In order to increase the statistical significance, data collection for PDF was carried out by progressively increasing the counting time with the diffraction angle. Further details are given in the SI. The signal of the empty kapton capillary was also recorded.

Further XRPD measurements were performed on selected samples:

- The XRPD pattern for PDF analysis was collected on sample Sm938 heat treated at 1000 °C as a reference mixed B- and C-type system.
- Nano samples with μ = 0.313, 0.344, and 0.375 were investigated at RT at the MSPD beamline of ALBA synchrotron, using a Mythen detector and λ = 0.41333 Å, Q_{max} = 25 Å^{-1}. The same sint Sm375 sample measured at the ESRF was investigated at ALBA at 90 K to check for reproducibility.

Compositional control of the powders was carried out through energy dispersive X-ray (EDX) analysis using a scanning electron microscope (Leo 1413) operating at 20 kV. EDX measurements were performed on four areas (1 mm × 1 mm in size) to check for material homogeneity.

2.3. Data Analysis. The average crystallographic structure was determined employing the Rietveld method[37] using the GSAS package.[38] The background was fitted with Chebyshev polynomials. Absorption correction was performed through the Lobanov empirical formula[39] for Debye−Scherrer geometry. Line profiles were fitted using a modified pseudo-Voigt function.[40]

At a first stage, one single atomic displacement parameter (adp) was attributed to all the ions, then a single adp per crystallographic site, still constraining O ions to the same value. In the case of C-type samples, anisotropic adps were employed on M sites to implement directional disorder.

The pair distribution function is described with the $G(r)$ formalism, which indicates the probability of finding a pair of atoms separated by a distance r. $G(r)$ is experimentally determined via sine Fourier transform of the total scattering function $F(Q)$:

$$G(r) = \frac{2}{\pi} \int_0^\infty F(Q)\sin(Qr)\, dQ \qquad (1)$$

PDF data were processed using the software PDFGetX2[41] and modeled through using PDFgui software,[42] which assesses the degree of accuracy of the refinement by the agreement parameter R_w:

$$R_w = \sqrt{\frac{\sum_{i=1}^n w(r_i)[G_{obs}(r_i) - G_{calc}(r_i)]^2}{\sum_{i=1}^n w(r_i)G_{obs}^2}} \qquad (2)$$

The analysis of conventional PDF from 2D detectors is generally limited to a few nanometers since the finite Q-space resolution reflects on the PDF signal as exponential damping of the intensity with the interatomic distance r.[43] The high resolution setup used in this study produces PDF with reliable signal up to hundreds of nanometers, thus allowing a multiscale investigation. This was conducted in PDFgui via the so-called boxcar refinements[43] in 20 Å wide boxes up to 500 Å with a 10 Å step.

Crystallite sizes were estimated through the Williamson−Hall method[44] employing at least 20 reflections for each calculation.

3. RESULTS AND DISCUSSIONS

Elemental analysis aimed at assessing the relative cation composition, since the nominal values are very close to each other. Actual compositions are slightly richer in Ce than nominally, thus suggesting excessive hydration of the Sm precursor. Since the variation is nearly systematic over the whole system, results and discussions refer to nominal compositions. Errors reported in Table 1 are the standard deviation of the elemental distribution probed in different regions.

Previous investigations on CeO_2 and Sm_2O_3 reported three main crystallographic phases, i.e. fluorite (F), C-type, and B-type.[23−25,45] The polymorphs are sketched in Figure 1 along with the best fit from Rietveld refinement. Cerium oxide (Figure 1a) exhibits fluorite (F) structure (space group $Fm\overline{3}m$, Ce 4a, 0, 0, 0 and O 8c, 1/4, 1/4, 1/4). Doping induced oxygen vacancies are randomly distributed on the O site in the long-range structure. Metal ions (M) are ideally 8-fold coordinated to oxygen at ∼2.34 Å (MO) and 12-fold coordinated to other cations at ∼3.8 Å (MM$_1$).

Sm_2O_3 sesquioxide was reported at ambient temperature either with C- or B-type structure.[23,45,46] The former (Figure 1b) has space group $Ia\overline{3}$ (Sm1 8b, 1/4,1/4,1/4; Sm2 24d, x, 0, 1/4; O1 48e, x, y, z) as observed in many other sesquioxides.[29,47] The two 6-fold coordinated cations exhibit
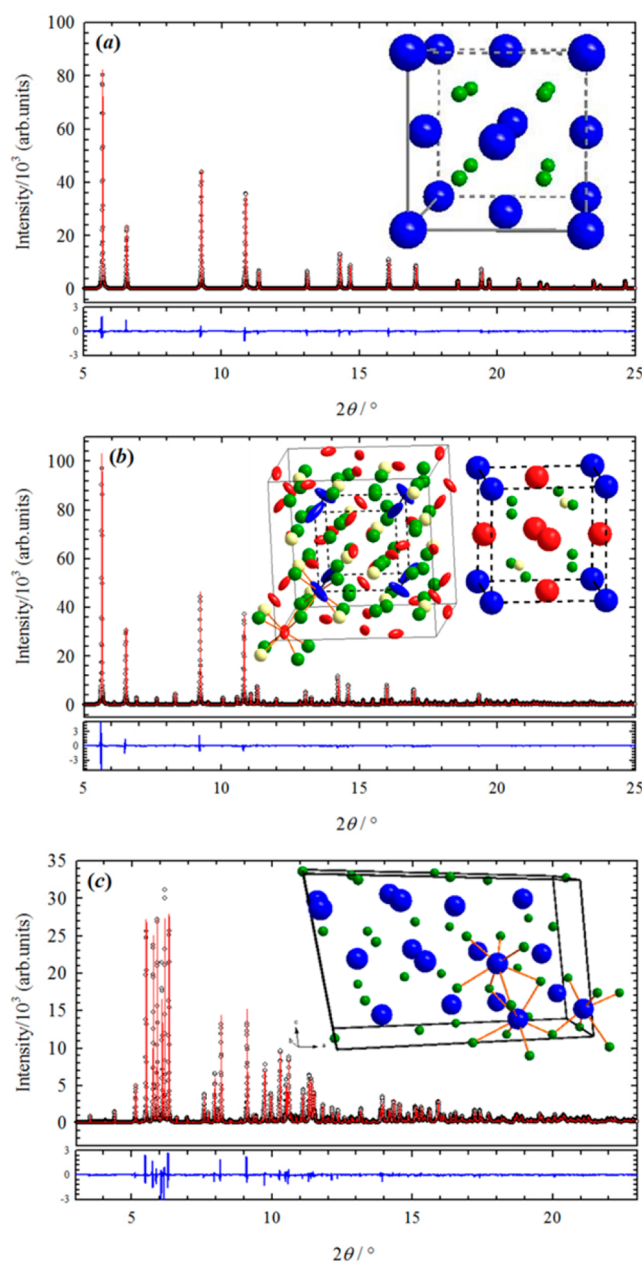

Figure 1. Rietveld refinements of the three crystallographic phases of interest in this study, the unit cell of which is displayed in the inset: (*a*) fluorite, Sm250; (*b*) C-type, Sm750; (*c*) B-type, Sm_2O_3. (*Rietveld refinements*) Empty circles experimental data, red solid lines calculated profile; blue residual. (*drawings*) Blue and dark green balls represent M and O ions, respectively. Orange sticks indicate the different M to O coordinations. In panel *b*, the size of the ellipsoids is proportional to the amplitude of adp. Different colors were selected for different Wickoff positions: blue M1, 8b; red M2, 24d; green O1, 48e; O2, 16c. Complete Rietveld refinements are reported in the SI.

two sets of cation−cation distances (MM$_1$ and MM$_2$), centered at ∼3.6 and ∼4.1 Å. C-type features a close relationship with fluorite: starting from the latter, a C-type phase can be obtained by doubling the cell axis, shifting the origin of (1/2, 1/2, 1/2) and displacing atomic coordinate from their special positions. A detailed overview is given in refs 14 and 15 where special attention is devoted to the x coordinate of the M2 site, i.e. x(M2). It represents the offset of the cation from the special position characteristic of fluorite,

Table 2. Results of Rietveld Refinements of Samples Investigated at the High Resolution Powder Diffraction Beamline of the ESRF for Four Compositional Regions (F, C*, C, B + C)[a]

μ(Sm)	0	0.125	0.250	0.3125
phase	F	F	F	F
a/Å	5.407196(2)	5.42136(1)	5.43504(5)	5.44129(2)
U(M)	0.00120(1)	0.00405(1)	0.00854(2)	0.01135(3)
U(O)	0.00347(3)	0.0081(1)	0.0152(2)	0.0180(3)
R(F²)	0.0281	0.0230	0.0337	0.0891
R_{wp}	0.0574	0.0514	0.0499	0.0595
size/nm		134(6)	82(2)	122(3)

μ(Sm)	0.4375	0.375	0.40625	0.4375
phase	C*	C*	C*	C*
a/Å	10.88899(9)	10.89125(6)	10.89691(5)	10.89954(5)
x(M2)	−0.00131(7)	−0.00471(6)	−0.00755(5)	−0.01067(5)
x(O1)	0.375	0.375	0.3798(7)	0.3802(7)
y(O1)	0.125	0.125	0.1348(6)	0.1384(7)
z(O1)	0.375	0.375	0.3779(10)	0.3802(8)
x(O2)	0.375	0.375	0.375	0.3794(14)
U11(M1)			0.0199(8)	0.0241(7)
U12(M1)			0.0172(5)	0.0212(5)
Uan(M1)	0.01325(4)[b]	0.01407(6)[b]	0.0199(8)	0.0241(7)
Uan(M2)	0.01325(4)[b]	0.01407(6)[b]	0.0147(3)	0.0138(2)
FWHM ratio	13.5(1.2)	3.7(2)	2.79(7)	1.91(6)
U(O)	0.0210(3)	0.0229(5)	0.0205(5)	0.0187(6)
R(F²)	0.0530	0.1338	0.0827	0.0936
R_{wp}	0.0716	0.0876	0.0961	0.0792
size/nm	135(2)	137(3)	153(4)	165(3)

μ(Sm)	0.500	0.5625	0.625	0.6875	0.750	0.8125
phase	C	C	C	C	C	C
a/Å	10.90639(4)	10.91253(2)	10.9164(2)	10.92300(2)	10.92294(3)	10.92402(2)
x(M2)	−0.01582(3)	−0.01762(3)	−0.01932(2)	−0.02103(2)	−0.02315(1)	−0.02519(2)
x(O1)	0.3845(3)	0.3810(3)	0.3825(3)	0.3830(3)	0.3835(3)	0.3859(2)
y(O1)	0.1392(3)	0.1444(3)	0.1452(3)	0.1470(2)	0.1469(3)	0.1471(2)
z(O1)	0.3841(4)	0.3781(5)	0.3783(4)	0.3791(3)	0.3786(4)	0.3802(3)
x(O2)	0.3817(9)	0.382(11)	0.3848(10)	0.380(2)	0.3841(11)	0.3865(9)
U11(M1)	0.0266(4)	0.0289(4)	0.02678(4)	0.0252(3)	0.0190(2)	0.01328(14)
U12(M1)	0.0192(4)	0.0202(4)	0.0188(4)	0.0172(3)	0.0136(2)	0.0098(2)
U11(M2)	0.00418(12)	0.0042(10)	0.00463(10)	0.00557(10)	0.00546(7)	0.00449(8)
U22(M2)	0.0138(3)	0.0124(2)	0.0103(2)	0.01052(16)	0.00895(11)	0.00669(12)
U33(M2)	0.0100(3)	0.0130(3)	0.0135(3)	0.0130(3)	0.0118(2)	0.0086(2)
U23(M2)	−0.0101(2)	−0.0110(2)	−0.00982(15)	−0.00858(14)	−0.00650(11)	−0.00420(12)
Uan(M1)	0.0266(4)	0.0289(4)	0.0268(4)	0.0252(3)	0.0190(2)	0.01328(14)
Uan(M2)	0.0093(3)	0.0099(2)	0.0095(2)	0.0097(2)	0.00872(13)	0.00660(13)
Uan(O)	0.0175(5)	0.0143(6)	0.0118(6)	0.0176(5)	0.0099(5)	0.0076(6)
FWHM ratio	1.14(2)	1.05(2)	1.05(1)	1.05(1)	1.01(1)	1.01(1)
R(F²)	0.0672	0.0500	0.0435	0.0340	0.0358	0.0212
R_{wp}	0.0807	0.0524	0.0577	0.0459	0.0441	0.0540
size/nm	170(5)	147(4)	136(3)	112(2)	107(2)	108(2)

μ(Sm)	0.875[c]	0.9375[d]	1
phase	C + B	C + B	C
a/Å	10.9256(8)	10.9255(2)	10.92595(5)
x(M2)	−0.02707(4)	−0.02876(7)	−0.03031(1)
x(O1)	0.3871(2)	0.3884(2)	0.3902(2)
y(O1)	0.1475(2)	0.1483(2)	0.1509(2)
z(O1)	0.3801(3)	0.3809(3)	0.3804(2)
x(O2)	0.3873(14)	0.383(2)	-
U11(M1)	0.0100(2)	0.0068(4)	0.00268(4)
U12(M1)	0.0091(4)	0.0075(7)	0.00095(9)
U11(M2)	0.00424(15)	0.0031(3)	0.00237(5)
U22(M2)	0.0054(2)	0.0037(4)	0.00219(8)
U33(M2)	0.0068(3)	0.0042(6)	0.00214(10)
U23(M2)	−0.0027(2)	−0.0014(4)	−0.00040(7)

Table 2. continued

$\mu(Sm)$	0.875[c]	0.9375[d]	1
Uan(M1)	0.0100(2)	0.0068(4)	0.00268(4)
Uan(M2)	0.0055(2)	0.0037(4)	0.00223(8)
Uan(O)	0.0091(9)	0.0054(17)	0.0061(4)
FWHM ratio	1.06(2)	1.04(2)	1.04(2)
R(F^2)	0.0196	0.0150	0.0209
R_{wp}	0.0476	0.0498	0.0515

[a]U stands for isotropic adp. Uan stands for the corresponding value of anisotropic adp in units of squared angstroms. FWHM ratio (see text for details) and crystallite size extracted through the WH method are also reported. [b]U(M1) and U(M2) constrained to the same value. [c]6.5(1) weight fraction of B-type phase. [d]19.3(1) weight fraction of B-type phase.
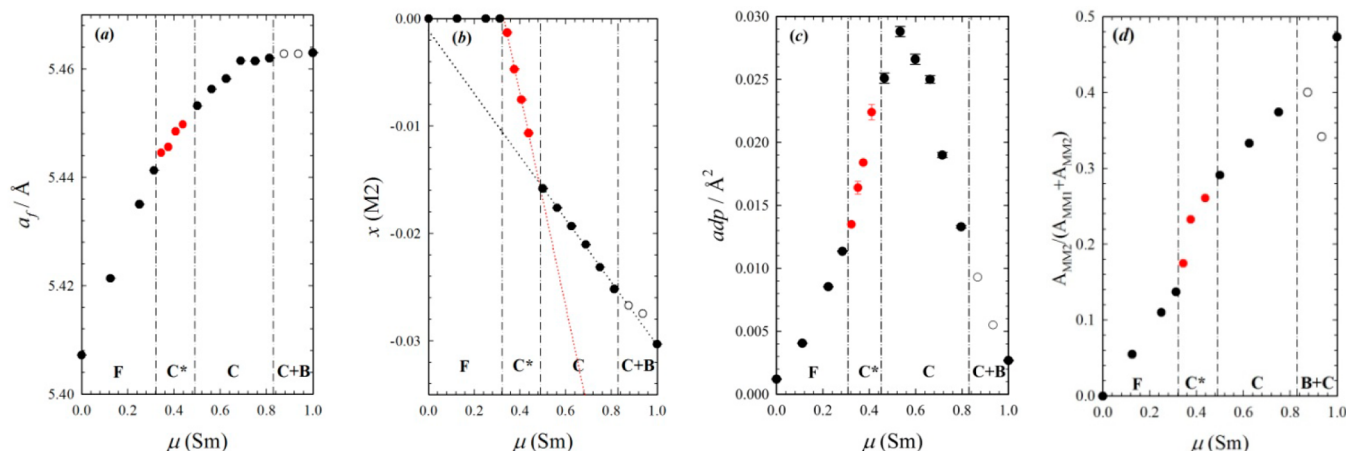
Figure 2. (a) a_f, (b) $x(M2)$, and (c) average adp obtained via Rietveld refinements for cubic phases. Full red and empty symbols highlight data across C* and biphasic C + B regions, respectively. (d) Relative intensity of the PDF peak at ~4.1 Å with respect to the MM$_1$ pair at ~3.8 Å. Dashed lines: boundary between different phases based on the trends, shown in dotted lines, in panel b. The values reported for pure Sm$_2$O$_3$ refer to the sample sintered at 700 °C for allowing comparisons with other cubic phases, since pure Sm$_2$O$_3$ sintered at 900 °C is nearly pure in B-type.

corresponding to $x(M2) = 0$. On the basis of previous investigations on doped-ceria compounds,[14,15,48] C-type samples characterized by small values of $x(M2)$ and peculiar microstructure will be labeled as C*.

The B-type polymorph (Figure 1c) of sesquioxides is monoclinic, space group $C2/m$. It is generally stabilized after high temperature annealing.[34,46,49] The structure is more complex than the other polymorphs: three cation sites are present, one 6-fold and two 7-fold coordinated to O ions, which occupy five different sites. The lower symmetry generates a number of different M−M distances: 16 lie between 3.7 and 3.8 Å, seven are displaced to 3.63 and 3.86 Å each, four at 4.17 Å, and two more at 3.34 Å.

3.1. Phase Evolution in the CeO$_2$−Sm$_2$O$_3$ System: General Observations. The phases obtained by Rietveld refinements are reported in Table 1, and structural parameters are reported in Table 2. By focusing on the sint series, the compositional phase evolution can be summarized as follows:

(i) $\mu \leq 0.313$: fluorite (F-type)
(ii) $0.344 < \mu < 0.500$: C* region
(iii) $0.500 \leq \mu \leq 0.813$: C-type
(iv) $0.875 < \mu < 1$: coexistence of C-type and B-type
(v) $\mu = 1$: B-type only

Following our previous investigations on Y[14] and Gd[15,28,50] dopants, the CeO$_2$−Sm$_2$O$_3$ system may be described with reference to the crystallographic relationship of F and C phases. Being the C-type lattice parameter double than fluorite, a reduced parameter a_f obtained by halving the cubic lattice parameter in the C-type region is reported in Figure 2a against

$\mu(Sm)$. The observed expansion is consistent with the larger ionic radius of Sm^{3+} (VII) with respect to Ce^{4+} (VIII), which are 1.02 and 0.97 Å, respectively.[51]

The evolution of $x(M2)$ with μ is reported in Figure 2b. It exhibits three linear trends corresponding to fluorite, C*, and C-type regions, with a deviation observed in the C-type region concomitant to the growth of the B-type phase.

The average adp determined from Rietveld refinements by constraining the adp of all ions to the same value is displayed in Figure 2c. The single adp values are given in Table 2. Three main aspects are to be considered: (i) adp show a bell-shape trend with $\mu(Sm)$ with maximum at approximately Sm500. This is inferred in terms of static disorder, typical of solid solutions of mixed oxides;[52,53] (ii) the magnitude of such an effect is remarkable: adp for intermediate compositions are about one order magnitude larger than those of the end-member compounds; (iii) adp of C-type samples have strongly anisotropic components; suggesting cations displacements toward the partially occupied O2 site. This agrees well with a previous investigation on Y-doped ceria,[14] where synchrotron and neutron diffraction data were used to study the environment of O^{2-} ions.

Crystallite sizes derived from the WH method are reported in Table 2. The sint powders have average particle size larger than 100 nm with a marked compositional dependence. Although WH gives just an approximation of the crystallite size, especially when far from the condition of a monodisperse size distribution, the current size values are consistent with those obtained by combined XRD and TEM on Gd-doped samples prepared after the same reaction pathway.[50] Nano

powders have average particle size is of ~15 nm, still consistent with previous investigations.[50]

The experimental PDF curves for all sint samples are displayed in Figure 3. Some selected F(Q) curves are shown in
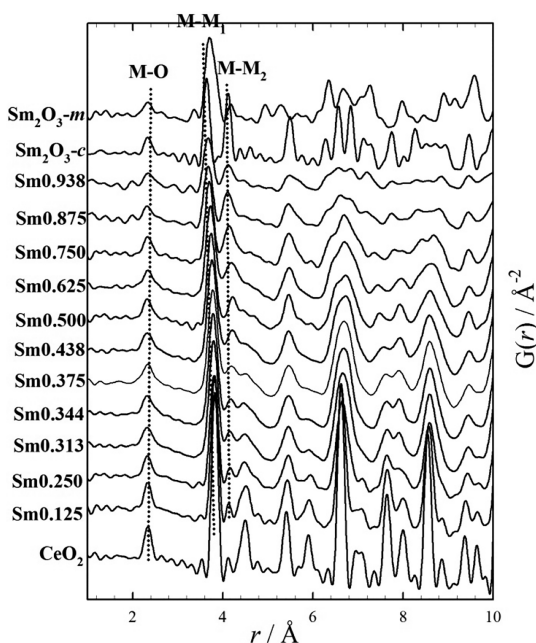

Figure 3. Experimental G(r) curves as computed using the PDFgetX2 software.

SI. A continuum of structural evolution is observed from CeO_2 to C-type Sm_2O_3. The atom pairs related to the main PDF peaks are reported in the same figure, where M indicates a site shared by both metal ions. O—O pairs are not observed as their contribution is negligible compared to the signal coming from atom pairs involving Ce and Sm atoms.

A characteristic feature of the PDF on doped ceria compounds is the peak at ~4.1 Å, labeled as MM_2, which is a signature of long M—M contacts in C-type.[29−56] It appears even for low doping amount, when the average structure is fluorite. The integrated area of the MM_2 peak normalized to the sum of both M—M contributions is reported in Figure 2d. It progressively increases with μ, and again, four different trends are observed.

The compositional evolution of the first atom pair (M—O) distance in the F region is reported in the SI. Although the addition of Sm into CeO_2 clearly promotes cell expansion, the first neighbor M—O distance shrinks with doping. This is at odds with fluorite structures, where all atoms lie in special positions and lattice expansion should lengthen all atom pairs. The same behavior was detected from EXAFS investigations.[24]

Both Rietveld refinements and PDF direct analysis show that the two transformations upon doping (i.e. F → C and C → B) exhibit different characteristics. Whereas cubic C and monoclinic B phases coexist for a large compositional region; no miscibility gap was found between F and C. This is made evident by the absence of splits in the structure peaks, which would arise in the case of long-range phase separation in Ce-rich fluorite and Sm-rich C-type phases. In the following, the two transformations characteristic of the CeO_2−Sm_2O_3 system will be described, first focusing on the C to B transition, then on that from F to C.

3.2. C to B Transformation.

Sint samples with composition $\mu \geq 0.875$ feature the presence, at least partial, of the monoclinic B phase. This is probed by the appearance of the characteristic peaks in XRPD patterns (see the SI), and it is further confirmed by deviations from the C-type local distances distribution observed in PDF in the same compositional range. Further information concerning the B to C phase equilibrium can be indirectly derived by the evolution of the C-type phase throughout the whole composition range. The saturation behavior of the a_f cell parameter observed for $\mu > \sim 0.7$ (Figure 2a) may suggest the achievement of the solubility limit of Sm into C-type, even though doped ceria compounds are well-known to deviate from Vegard's law.[57] In fact, x(M2) decreases linearly and only with formation of B-type ($\mu \geq 0.875$) a weak deviation from the linear trend is observed (Figure 2b). Being x(M2) strictly related to the amount of oxygen vacancies within the C-type phase, this finding suggests that the transformation from C- to B-type of part of the sample reduces the amount of oxygen vacancies in the C-type phase compared to a fully C-type material.

The B-type phase fraction depends also on the annealing temperature. When treated at 700 °C, Sm_2O_3 was obtained nearly pure C-type. A set of different thermal treatments was performed to evaluate the progressive transformation from C- to B-type. Full experimental details and results are reported in the SI. The main findings are the following:

- The C to B transformation occurs irreversibly.
- Sm750 is the richest composition in Ce not transforming into B type even for prolonged high temperature annealing.
- Full B-type is obtained only after 3 days annealing Sm_2O_3 at least at 900 °C.
- For intermediate compositions and annealing temperatures, the B-type content increases progressively with μ and temperature.

The latter effect is opposite to what one would expect based on symmetry considerations, but it has been already observed on the pure oxide; see ref 58 and references therein.

In view of the above results, the B-type phase may be deemed as the thermodynamically stable form for $\mu \geq 0.875$, but it requires long times and high temperature for complete transformation. The compositional range of the transformation is consistent with the work of Nitani et al.,[24] who reported a biphasic C and B system for $0.8 \leq \mu \leq 0.9$ from solid state reaction carried out at 1400 °C.

The C- to B-type transformation affects also real space data. The onset of the B-type phase gives an additive contribution to the shorter cation−cation distance MM_1 (see pure monoclinic Sm_2O_3 PDF on the top of Figure 3), thus decreasing the intensity ratio between the two M—M pairs (empty circles in Figure 2d) which goes out of the trend of C-type samples. As these biphasic samples are richer in C-type phase which has higher symmetry than B-type, the contribution of B-type to PDF is nearly negligible. In order to have a representative picture of the short and intermediate scale relationship between B and C type, a sample with larger B-type content was chosen (38 wt %), which was produced by annealing Sm938 at 1000 °C for 3 days (see the SI). The corresponding PDF turned out to be consistent with the average scale modeling from Rietveld refinements, i.e. it can be modeled as the coexistence of B- and C-type from the local scale up to tens of nanometers. The local scale modeling is shown in Figure 4a,
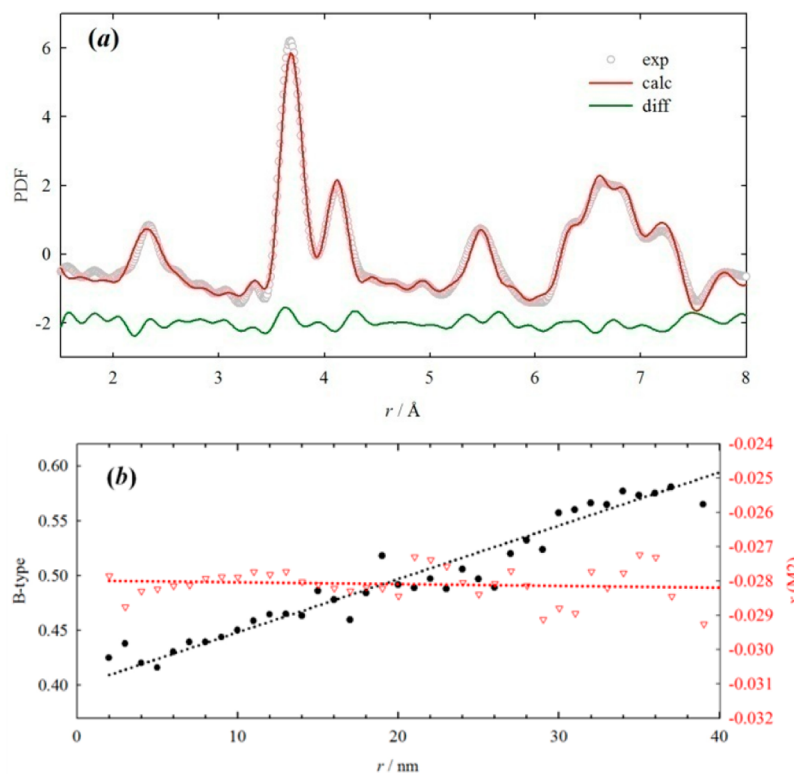
Figure 4. (*a*) PDF refinement of sample Sm938 heated at 1000 °C for 3 days in the region 1.5 < *r* < 8 Å considering coexistence of phases B and C: empty circles experimental data; red solid lines calculated; green solid lines residual. (*b*) Output of boxcar refinement on the sample: (full black circles, left-hand axis) relative amount of the B phase; (empty red triangles, right-hand axis) *x*(M2) as a function of the interatomic distance *r*.
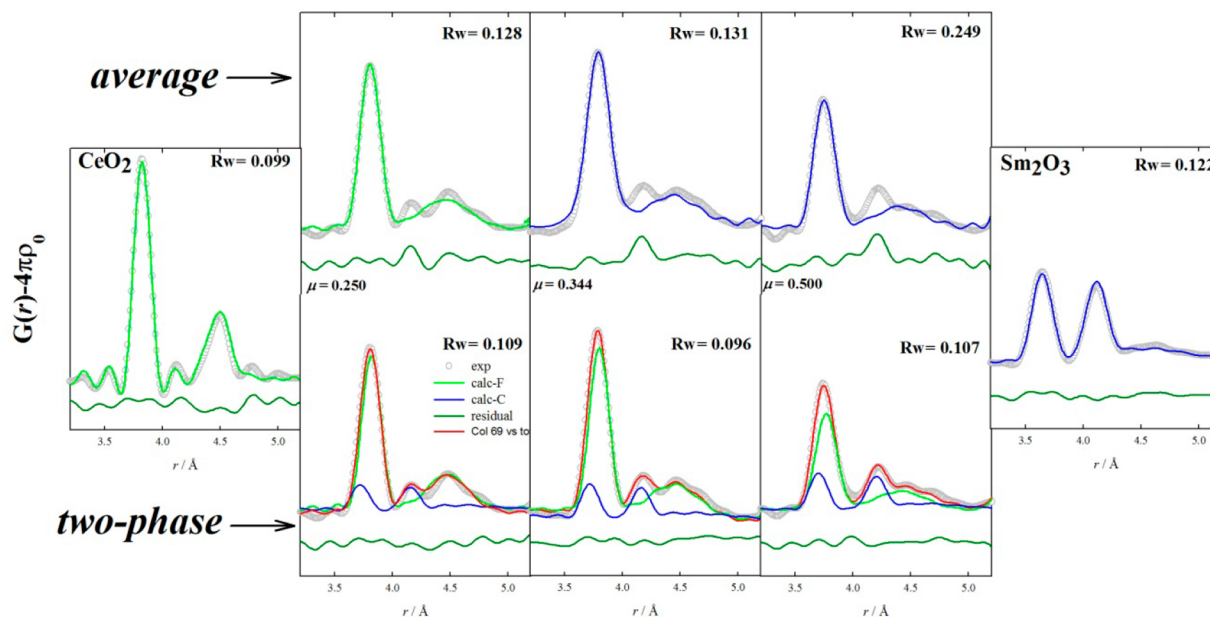

Figure 5. PDF refinements using average (top) and two-phase (bottom) models for the pure oxides and some selected compositions: empty circles experimental data; green solid lines calculated contribution of fluorite, blue solid lines calculated contribution of C-type; red solid lines overall calculated profile. The difference curves are shown below each pattern.

where for statistical significance only a limited number of parameters was refined, i.e. lattice parameters, relative scale factors, one adp for cations, and one for anions, with all atomic coordinated constrained to the values of the average structure, but *x*(M2) of C-type.

The same procedure was applied through boxcar refinements up to 40 nm. The values of *x*(M2) and the relative amount of the B-type phase are displayed in Figure 4*b*. *x*(M2) oscillates around −0.028 for the full *r*-range investigated, in agreement with Rietveld analysis. This suggests no intermediate scale ordering between B- and C-type phases, that

would otherwise affect $x(M2)$. The only structural parameter that evolves with the interatomic distance r is the relative amount of the two phases.

The B-type phase, which is stabilized only after high temperature annealing, shows sharper peaks in the Q-space patterns. This indicates that its crystals are bigger than those of C-type, and/or they are affected by less strain, as a consequence of the high temperature treatment. Both effects are supposed to deplete C-type interatomic distances in the long-range PDF, which is probed as increase of B-type phase with r (Figure 4b).

In conclusion, all the above findings provide evidence of a complete long-range separation between C- and B-type which is reminiscent of a first order transition induced both by temperature and by doping.

3.3. F to C Region. According to the $x(M2)$ evolution reported in Figure 2b, the compositional limit of fluorite upon Sm doping can be determined as the intercept of the linear trends of $x(M2)$ in the C* region against $x(M2) = 0$ of fluorite.[14] Sm solubility limit turns out to be $\mu \sim 0.32$, indeed sample Sm313 has $x(M2) = 0$ and it shows no evidence of superstructure peaks. Using the same approach, the limit between C* and C regions is set at $\mu \sim 0.49$.

A very similar dependence is given by the normalized intensity of MM_2 PDF peak (Figure 2d). The relative peak intensity increases already within the F region, it shows a sudden increase in the C* region, then it continues to slope linearly for $\mu > 0.500$. This is concomitant to the steep increase of adp, a fingerprint of static disorder linked to the presence of C-type like atomic arrangements as already reported for other doped ceria compounds.[29]

Figure 5 displays the output of nonlinear least-squares refinements performed on the short-range PDF of some selected compositions, by employing the average crystallographic structure (top) and the coexistence of F and C phases (bottom), the latter called the "biphasic model" with green and blue solid lines showing separately the calculated contributions of F- and C-type, respectively. Details on refinement strategy are reported elsewhere.[48,59] Except for the end-member compounds, the average model fails describing the experimental data. The biphasic model provides the best fit for all doped samples in the $\mu \leq 0.750$ range. It can be pictured as the formation of C-type distorted regions rich in dopant and oxygen vacancies, defined as droplets, embedded in a fluorite matrix, as already observed for other dopants.[28,29] The C-type phase fractions returned by the fit are given in Table 3 together with $x(M2)$ and the fit residual R_w from average (R_w av) and biphasic (R_w biph) modeling. Compared to PDF, Rietveld refinements returned $x(M2)$ much smaller in magnitude, especially for F and C* regions, as $x(M2)$ is averaged over the CeO_2 matrix and the droplets rich in Sm^{3+}, therefore in O vacancies. Instead, PDF refers only to the C-type phase at the local scale, hence it probes larger $x(M2)$ values.

The extent of the domains rich in oxygen vacancies was estimated by monitoring the r-distance dependence of $x(M2)$ using the strategy described in ref 48. Since a single C-type phase is considered for this purpose, $x(M2)$ is averaged over fluorite ($x(M2) = 0$) and C-type ($x(M2) < 0$) regions, therefore it is less negative than for the biphasic model.

The evolution of $x(M2)$ as a function of the interatomic distances for the sint series is reported in Figure 6a. Whereas $x(M2)$ for C-type samples is constant with r (see Sm500), for C* samples it goes to zero within some nanometers. This

Table 3. Output of Real Space Refinements Performed in the Interatomic Range 1.5 < r < 5.2 Å Using a Biphasic Model[a]

μ(Sm)	C frac	R_w av	R_w biph	$x(M2)/r$ space	$x(M2)/Q$ space
0.125	0.150(5)	0.135	0.110	−0.0266(4)	0
0.250	0.225(3)	0.128	0.109	−0.0264(4)	0
0.313	0.240(3)	0.160	0.091	−0.0273(3)	0
0.344	0.260(4)	0.201	0.096	−0.0279(3)	−0.00131(7)
0.375	0.294(3)	0.207	0.096	−0.0291(3)	−0.00471(6)
0.438	0.341(3)	0.229	0.112	−0.0310(3)	−0.01067(5)
0.500	0.401(2)	0.345	0.107	−0.0315(4)	−0.01582(3)
0.625	0.467(4)	0.311	0.123	−0.0308(2)	−0.01932(2)
0.750	0.645(2)	0.317	0.134	−0.0288(3)	−0.02315(1)

[a]The $x(M2)$ values from Q-space analysis are added to the table to facilitate comparisons.
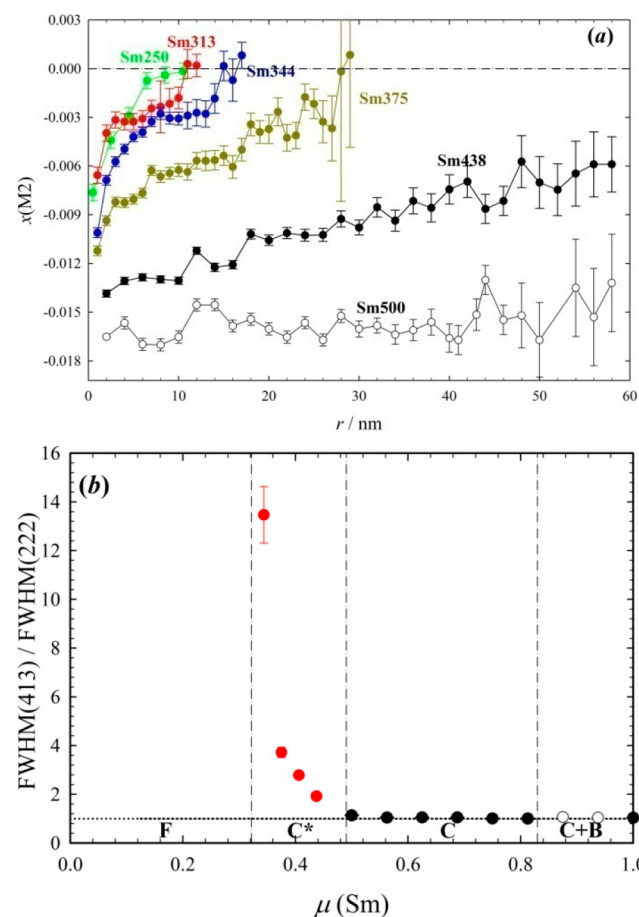

Figure 6. (a) $x(M2)$ as a function of interatomic distance r evaluated using a single C-type phase. (b) Compositional evolution of FWHM ratio.

recalls the picture of C-type nanodomains within a fluorite matrix: for interatomic distances larger than the nanodomain size, no direct structural correlation exists and $x(M2)$ averages out to zero. Conversely, when interatomic distances lie within the C-type nanodomain, $x(M2) \neq 0$ and even for Sm125 the local $x(M2)$ is very similar to that of pure Sm_2O_3 (see Table 3). Hence, one can consider the extent of the C-type domains to be as large as the r value at which $x(M2)$ goes to zero. Domain sizes of 10, 11, 15, and 28 nm were estimated for μ = 0.250, 0.313, 0.344, and 0.375, respectively. Besides the static disorder evidenced by the μ dependence of adp, nanodomains

Table 4. C-Type Domain Size Estimated by PDF, C-Type Fractions (Droplets), and APB Probability for Sm (This Study), Gd,[15] and Y[14] Doping for Different Dopant Concentrations[a]

	Sm			Gd[15]			Y[14]		
μ	domains	droplets	APB	domains	droplets	APB	domains	droplets	APB
0.250	10	0.23		12	0.20		12	0.24	
0.313	11	0.24		23	0.26	0.135(8)	14	0.26	0.12(2)
0.344	15	0.26	0.35(3)	40	0.30	0.044(1)	18	0.30	0.080(4)
0.375	28	0.29	0.068(2)	>50	0.30	0.030(1)			0.048(2)
0.438	>50	0.37	0.021(1)	>50	0.37	0.0032(2)	>50	0.37	0.006(3)

[a]Uncertainties for the droplets were estimated to be ~0.01, for domains ~1 nm.

affect the experimental XRPD patterns in terms of broadening of superstructure peaks in C* samples. Figure 6b reports the ratio between the full width at half maximum of the selected (413) (superstructure) to the (222) (structure) reflection. This parameter is listed in Table 2 as FWHM ratio. The ratio increases for $\mu < 0.500$, i.e., in the C* region, while for $\mu > 0.500$ it is ~1. The maximum is observed at $\mu = 0.344$, concomitant to the long-range growth of C-type phase. This behavior is associated to the formation of antiphase boundary (APB), which are the only defects accounting for the broadening of superstructure peaks only: neither particle size, nor the coexistence of fluorite and nanometric C-type may correctly model the experimental pattern. An example of a successful refinement by pm2k software[60] on Sm344 is shown in the SI. APB probabilities for all compositions are given in Table 2.

3.3.1. Comparisons with Gd and Y Doping. Sm is acknowledged as one of the best possible dopants for CeO_2 together with Y and Gd.[18,19] Compared to Gd[15] and Y,[14] Sm doping affects similarly the defect structure of CeO_2, as disorder is mainly driven by the formation and ordering of oxygen vacancies on a large scale. On the other side, the effect of the type of dopant is more subtle.

First off, lattice parameters reflect the ionic radii of the dopant: a clear lattice expansion is experienced after Gd-, and to a larger extent, Sm doping, whereas Y induces only a very slight contraction, especially as concerns fluorite samples, in agreement with tabulated values.[25] In view of the application as ionic conductor, Y doping seems to be the best choice, since it reduces the lattice strain compared to pure CeO_2, according to the similarity of ionic radii between Y^{3+}(VII) and Ce^{4+}(VIII).[51]

On the other hand, the trend of $x(M2)$ with the composition suggests that Sm has a larger solubility into fluorite (~0.32) with respect to Gd and Y, i.e., ~0.28 and ~0.27, respectively. Yet, long-range fluorite is not a necessary condition for high-performance ionic conductors. As an example, La doping stabilizes fluorite up to $\mu(La) = 0.50$,[61] still La is known to be far from high performance, from an experimental[62] and theoretical[63] basis. It follows that rather than the average structure, local, and mesoscopic orderings are to be taken into account.

The average domain size for different dopants and compositions is summarized in Table 4. For $\mu = 0.25$, the three dopants exhibit similar hierarchical structure, hosting C-type domains of ~10 nm. For larger dopant amounts, Gd exhibits much bigger domain sizes, while Sm still gives smaller domain sizes compared to Y. According to the work of Kilner[5] and references therein, to a first approximation, the activation energy for oxygen migration has two main contributions: the enthalpy of migration and the interactions involving oxygen vacancies. Sm turned out to have the lowest tendency to form

aggregates, therefore it can be preferred, on a structural basis, as a dopant in ceria for SOFCs application. According to the same principle, Y should be more suitable than Gd.

3.3.2. Nanometric Doped Ceria. Trivalent doping of CeO_2 results in the formation of domains in the order of tens of nanometers depending on sample stoichiometry. These defect structures, which strongly distort the original fluorite lattice, are supposed to be the prime source for the conductivity drop with dopant concentration. A possible way to modify the C-type domain distribution is to produce nanoparticles having size similar or smaller than the domains. In this case, one could expect either the dopant ions still forming some particles full C-type and others full fluorite[64] or the dopants distributing randomly all over the particles.

In order to verify these hypotheses, we collected PDF data on nano C* samples at the MSPD beamline at ALBA, which is equipped with a fast recording Mythen detector. Sample Sm375 was measured at the same low temperature on both beamlines for reproducibility, and it gave very similar PDF curves, which are shown in the SI.

The effect of the crystallite size on Q and real space patterns of Sm375 are displayed in Figure 7a and b, respectively. The particle size were found to be 14(2), 13(2), and 14(1) nm for samples $\mu = 0.313$, 0.344, and 0.375, respectively. Sm375 nanocrystals already exhibit some superstructure peaks, which were not observed in samples with smaller Sm amount. These superstructure peaks are though very broad and their accurate analysis, in terms of FWHM, is difficult. Rietveld refinements suggest that nano Sm375 has $x(M2)$ smaller in magnitude than sint Sm375 (see Table 5), while $x(M2)$ for nano Sm344 is too close to zero to discern the structure from fluorite.

The PDF curves reported in panel b highlight deviations between Sm375 nano and sint, especially within 10 Å. In particular, the M−M pair at ~4.1 Å is more intense in the case of the sintered sample. This suggests that the formation of C-type droplets in nanoparticles is limited, consistently with equivalent Gd-doped samples.[50] This is confirmed by the C-type fractions reported in Table 5, which are systematically smaller than the equivalent sint reported in Table 3.

Figure 7c displays the evolution of $x(M2)$ with r for samples nano. All exhibit C-type features well beyond the first coordination shell, with $x(M2)$ vanishing faster for smaller μ. The structure of the nanoparticles has to be figured out by combining all available information.

Sample Sm375 nano has C-type structure as the corresponding sint powder. This is testified by the occurrence of superstructure peaks (inset of Figure 7a) and by $x(M2)$ from PDF different than zero throughout the full length of the crystals (Figure 7c). Although both samples are on average C-type, they have different microstructure. Nanopowders (~14 nm) are fully C-type with $x(M2)$ ~−0.0022 from Rietveld,
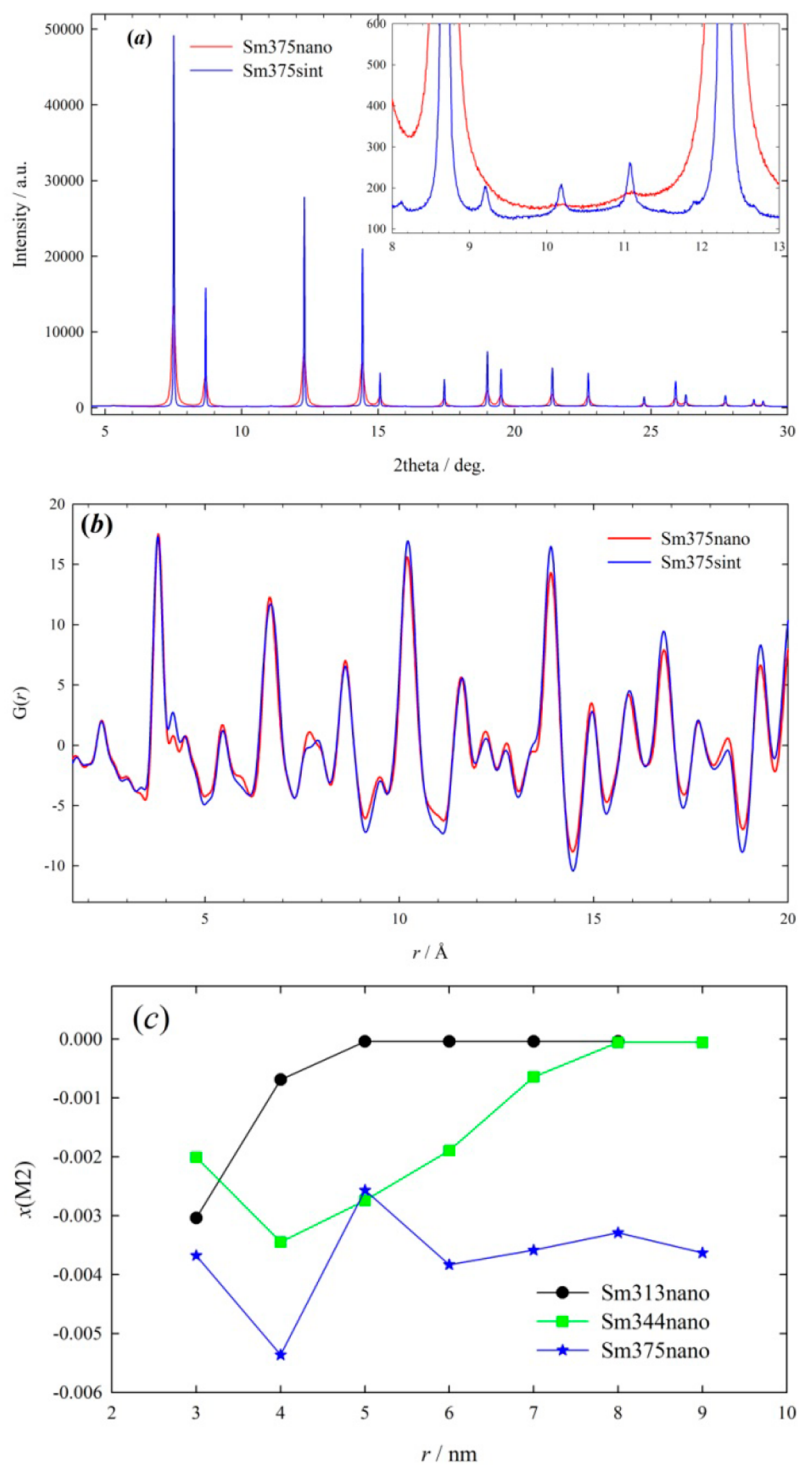
Figure 7. (*a*) Experimental patterns collected at MSPD on sample Sm375 nano (red) and sint (blue) and (*b*) corresponding G(*r*) curves. (*c*) *x*(M2) as a function of the interatomic distances for Sm313 (black circles), Sm344 (green squares), and Sm375 (blue stars) fired at 500 °C. The esd are not reported in panel *c*; they can be assumed to be ∼0.001.

while the sint equivalent is composed of nanodomains ∼30 nm wide percolated through the fluorite matrix. These nanodomains have stronger C-type distortion, (*x*(M2) = −0.0045) compared to nanocrystals. A very similar process was observed for Gd doping,[50] suggesting that such a mechanism might apply in general to trivalent dopants in ceria.

Reducing Sm-amount makes hard the assessment of the crystallographic structure, as peaks are too broad to state

unambiguously whether the long-range structure is C-type or fluorite. The PDF of Sm344 shows the progressive vanishing with *r* of *x*(M2). Since *x*(M2) is very small in magnitude, the discernment between F and C-type is not straightforward, especially as the *r*-decay of the PDF signal decreases the accuracy of *x*(M2). This picture can be defined as a sort of hybrid structure, as proposed in refs 26, 45, and 65 very similar to fluorite, even though having characteristics typical of the C-

Table 5. Output of PDF Refinements Performed on C* Samples at the MSPD Beamline at ALBA in the Interatomic Range 1.5 < r < 5.2 Å

x(RE)	series	C-type frac	x(M2)/r-space	x(M2)/Q-space	R_w biphasic
0.313	nano	0.190(1)	−0.0245(1)	0	0.118
0.344	nano	0.249(1)	−0.0250(1)	0	0.107
0.375	nano	0.279(1)	−0.0278(1)	−0.0021(2)	0.112
0.375	sint	0.291(2)	−0.0290(2)	−0.00504(6)	0.116

type phase. In alternative, it could indicate the presence of very small nanodomains with different orientations even in Sm344 nano.

As concerns Sm313 nano, x(M2) from PDF goes very fast to zero. As the sint equivalent is fully fluorite with no superstructure peaks and x(M2) is close to zero, Sm313 nano can be defined as fluorite, with some C-type ordering acting as a seed for the growing of the C-type domains at a higher temperature.

In conclusion, regardless of the morphology and the length scale considered, the fluorite to C-type transformation occurs continuously with doping. x(M2) can be inferred as an optimal order parameter in the context of a second order phase transition. However, since the definition of the transition character, i.e. displacive or order−disorder, as well as the evolution of the distortion modes associated with irreducible representations are beyond the scope of the present study; this topic will be discussed in a dedicated paper.

4. CONCLUSIONS

This study presents a complete structural investigation on different length scales of the full CeO_2−Sm_2O_3 system.

Two different phase transformations are observed as a function of the Sm/Ce ratio: starting from the fluorite structure of CeO_2, Sm-addition first leads to a C-type phase, then, for high Sm-contents, to a monoclinic B-type phase. Although both transformations are well-known to occur in the CeO_2−Sm_2O_3 system, the present investigation demonstrates that they are different in nature.

The irreversible C to B-type phase transformation of Sm_2O_3 occurring during high temperature annealing ($T \geq 900$ °C) strongly suggests that the monoclinic phase is the thermodynamically stable form of Sm_2O_3. The same applies to compositions $\mu \geq 0.875$, which show the formation of some B phase after high temperature annealing. The residual C-type phase is probably a consequence of a very slow kinetic. The PDF investigation confirmed a complete separation between the two phases and the G(r) curves are better described with a mix of B- and C-type phases whatever the length scale.

The F- to C-type transformation shows a different behavior; none of the high resolution XRPD patterns probed the coexistence of both phases. Intermediate compositions, though, exhibit very strong disorder, quantified as an increase of adp by an order of magnitude, together with the broadening of superstructure peaks.

Rather than a complete phase separation, increasing Sm doping into ceria promotes a complex defect ordering, which features (i) locally the formation of randomly oriented droplets (dopant- and oxygen vacancy-rich aggregates with distorted C-type phase, consistent with absorption spectroscopy results[24,62]) even for low doping amounts and long-range fluorite phase, whose concentration increases with Sm amount;

(ii) the droplets average into domains with a size of tens of nanometers, (iii) after a critical threshold, located in the range 0.313 < μ < 0.344, domains grow in size and percolate throughout the crystallites. Since the operation of the electrolytes in SOFC is related to the ability of O^{2-} ions to migrate through the doping-induced vacancies, the trap of oxygen vacancies in C-type droplets and domains is likely the reason of the conductivity drop with concentration. Indeed, the same picture of disorder evolution across the F- to C-type phase transformation was observed when employing other doping elements, such as Y[14] and Gd.[15,28]

In this context, the present investigation aimed at defining which structural conditions for doped ceria electrolytes is suitable for ionic migration. Among the three dopants, Sm is the one which exhibits, for most of the concentrations considered, smaller C-type domains.

Qualitatively, the same scheme of hierarchical defect structure applies also to the crystals in their nanometric form. Smaller amounts of Sm doping, though, are required to obtain full C-type phase in nanocrystals. This effect is compensated by the slightly enhanced fluorite character of C-type compared to sintered samples.

■ ASSOCIATED CONTENT

Ⓢ Supporting Information

The Supporting Information is available free of charge on the ACS Publications website at DOI: 10.1021/acs.inorg-chem.7b02896.

Details of Rietveld refinements, F(Q) curves, M−O distances from PDF, effect of temperature and aging on the C to B transformation, refinement of antiphase boundaries domains, and comparison of PDF collected from the same sample on different instruments (PDF)

■ AUTHOR INFORMATION

Corresponding Author

*E-mail: codurimauro@gmail.com.

ORCID Ⓘ

Mauro Coduri: 0000-0002-5387-8947

Notes

The authors declare no competing financial interest.

■ ACKNOWLEDGMENTS

■ REFERENCES

(1) Steele, B. C. H. Appraisal of $Ce_{1-y}Gd_yO_{2-y/2}$ electrolytes for IT-SOFC operation at 500 C. *Solid State Ionics* **2000**, *129*, 95−110.

(2) Michel, D.; Perez y Jorba, M.; Collongues, R. Study by Raman spectroscopy of order-disorder phenomena occurring in some binary oxides with fluorite-related structures. *J. Raman Spectrosc.* **1976**, *5*, 163−180.

(3) Malavasi, L.; Fisher, C. A. J.; Islam, S. Oxide-ion and proton conducting electrolyte materials for clean energy applications: structural and mechanistic features. *Chem. Soc. Rev.* **2010**, *39*, 4370−4387.

(4) Małecka, M. A. Ceria-based mixes oxides - beautiful structures. *Chemistry Select* **2016**, *1*, 4246−4254.

(5) Kilner, J. A. Defects and Conductivity in Ceria-based Oxides. *Chem. Lett.* **2008**, *37*, 1012−1015.

(6) Kilner, J. A. Fast oxygen transport in acceptor doped oxides. *Solid State Ionics* **2000**, *129*, 13–23.

(7) Bevan, D. J. M.; Kordis, J. Mixed oxides of the type MO$_2$ (fluorite)—M$_2$O$_3$—I oxygen dissociation pressures and phase relationships in the system CeO$_2$-Ce$_2$O$_3$ at high temperatures. *J. Inorg. Nucl. Chem.* **1964**, *26*, 1509–1523.

(8) Kim, D.-J. Lattice Parameters, Ionic Conductivities, and Solubility Limits in Fluorite-Structure MO2 Oxide [M = Hf^{4+}, Zr^{4+}, Ce^{4+}, Th^{4+}, U^{4+}] Solid Solutions. *J. Am. Ceram. Soc.* **1989**, *72*, 1415–1421.

(9) Deguchi, H.; Yoshida, H.; Inagaki, T.; Horiuchi, M. EXAFS study of doped ceria using multiple data set fit. *Solid State Ionics* **2005**, *176*, 1817–1825.

(10) Ohashi, T.; Yamazaki, S.; Tokunaga, T.; Arita, Y.; Matsui, T.; Harami, T.; Kobayashi, K. EXAFS study of Ce$_{1-x}$Gd$_x$O$_{2-x/2}$. *Solid State Ionics* **1998**, *113–115*, 559–564.

(11) Kim, N.; Stebbins, J. F. Vacancy and Cation Distribution in Yttria-Doped Ceria: An ^{89}Y and ^{17}O MAS NMR Study. Chem. *Chem. Mater.* **2007**, *19*, 5742–5747.

(12) Mori, T.; Wang, Y.; Drennan, J.; Auchterlonie, G.; Li, J.-G.; Ikegami, T. Influence of particle morphology on nanostructural feature and conducting property in Sm-doped CeO$_2$ sintered body. *Solid State Ionics* **2004**, *175*, 641–649.

(13) Ye, F.; Mori, T.; Ou, D. R.; Zou, J.; Auchterlonie, G.; Drennan, J. Compositional and structural characteristics of nano-sized domains in gadolinium-doped ceria. *Solid State Ionics* **2008**, *179*, 827–831.

(14) Coduri, M.; Scavini, M.; Allieta, M.; Brunelli, M.; Ferrero, C. Defect structure of Y-doped ceria on different length scales. *Chem. Mater.* **2013**, *25*, 4278–4289.

(15) Scavini, M.; Coduri, M.; Allieta, M.; Masala, P.; Cappelli, S.; Oliva, C.; Brunelli, M.; Orsini, F.; Ferrero, C. Percolating hierarchical defect structures drive phase transformation in Ce$_{1-x}$Gd$_x$O$_{2-x/2}$: a total scattering study. *IUCrJ* **2015**, *2* (5), 511–522.

(16) Purton, J. A.; Allan, N. L.; Gunn, D. S. D. Simulations of doped CeO 2 at finite dopant concentrations. *Solid State Ionics* **2017**, *299*, 32–37.

(17) Purton, J. A.; Archer, A.; Allan, N. L.; Gunn, D. S. D. Growth of nano-domains in Gd–CeO2 mixtures: hybrid Monte Carlo simulations. *J. Mater. Chem. A* **2016**, *4*, 4592–4602.

(18) Eguchi, K.; Setoguchi, T.; Inoue, T.; Arai, H. Electrical properties of ceria-based oxides and their application to solid oxide fuel cells. *Solid State Ionics* **1992**, *52*, 165–172.

(19) Mogensen, M.; Sammes, N. M.; Tompsett, G. A. Physical, chemical and electrochemical properties of pure and doped ceria. *Solid State Ionics* **2000**, *129*, 63–94.

(20) Zha, S.; Xia, C.; Meng, G. Effect of Gd (Sm) doping on properties of ceria electrolyte for solid oxide fuel cells. *J. Power Sources* **2003**, *115*, 44–48.

(21) Jung, G.-B.; Huang, T.-J.; Chang, C.-L. Effect of temperature and dopant concentration on the conductivity of samaria-doped ceria electrolyte. *J. Solid State Electrochem.* **2002**, *6*, 225–230.

(22) Huang, W.; Shuk, P.; Greenblatt, M. Properties of sol-gel prepared Ce$_{1-x}$Sm$_x$O$_{2-x/2}$ solid electrolytes. *Solid State Ionics* **1997**, *100*, 23–27.

(23) Mandal, B. P.; Grover, V.; Tyagi, A. K. Phase relations, lattice thermal expansion in Ce$_{1-x}$Eu$_x$O$_{2-x/2}$ and Ce$_{1-x}$Sm$_x$O$_{2-x/2}$ systems and stabilization of cubic RE$_2$O$_3$ (RE: Eu, Sm). Materials Science and Engineering. *Mater. Sci. Eng., A* **2006**, *430*, 120–124.

(24) Nitani, H.; Nakagawa, T.; Yamanouchi, M.; Osuki, T.; Yuya, M.; Yamamoto, T. A. XAFS and XRD study of ceria doped with Pr, Nd or Sm. *Mater. Lett.* **2004**, *58*, 2076–2081.

(25) Eyring, L. *Handbook on the Physics and Chemistry of Rare Earths*; Gschneidner, K. A., Jr., Eyring, L., Eds.; Elsevier: Amsterdam, 1979; Vol. 3, pp 337–399.

(26) Artini, C.; Pani, M.; Carnasciali, M. M.; Buscaglia, M. T.; Plaisier, J. R.; Costa, G. A. Structural Features of Sm- and Gd-Doped Ceria Studied by Synchrotron X-ray Diffraction and μ-Raman Spectroscopy. *Inorg. Chem.* **2015**, *54*, 4126–4137.

(27) Artini, C.; Pani, M.; Carnasciali, M. M.; Plaisier, J. R.; Costa, G. A. Lu-, Sm-, and Gd-Doped Ceria: A Comparative Approach to Their Structural Properties. *Inorg. Chem.* **2016**, *55*, 10567–10579.

(28) Scavini, M.; Coduri, M.; Allieta, M.; Brunelli, M.; Ferrero, C. Probing Complex Disorder in Ce$_{1-x}$Gd$_x$O$_{2-x/2}$ Using the Pair Distribution Function Analysis. *Chem. Mater.* **2012**, *24*, 1338–1345.

(29) Coduri, M.; Brunelli, M.; Scavini, M.; Allieta, M.; Masala, P.; Capogna, L.; Fischer, H. E.; Ferrero, C. Rare Earth doped ceria: a combined X-ray and neutron pair distribution function study. *Zeitschrift für Kristallographie* **2012**, *227*, 272–279.

(30) Coduri, M.; Scavini, M.; Brunelli, M.; Pedrazzin, E.; Masala, P. Structural characterization of Tb- and Pr-doped ceria. *Solid State Ionics* **2014**, *268*, 150–155.

(31) Sardar, K.; Playford, H. Y.; Darton, R. J.; Barney, E. R.; Hannon, A. C.; Tompsett, D.; Fisher, J.; Kashtiban, R. J.; Sloan, J.; Ramos, S.; Cibin, G.; Walton, R. I. Nanocrystalline Cerium-Bismuth Oxides: Synthesis, Structural Characterization, and Redox Properties. *Chem. Mater.* **2010**, *22* (22), 6191–6201.

(32) Gateshki, M.; Niederberger, M.; Deshpande, A. S.; Ren, Y.; Petkov, V. Atomic-scale structure of nanocrystalline CeO$_2$–ZrO$_2$ oxides by total x-ray diffraction and pair distribution function analysis. *J. Phys.: Condens. Matter* **2007**, *19*, 156205.

(33) Coduri, M.; Scavini, M.; Brunelli, M.; Masala, P. In situ pair distribution function study on lanthanum doped ceria. *Phys. Chem. Chem. Phys.* **2013**, *15*, 8495–8505.

(34) Zinkevich, M. Thermodynamics of rare earth sesquioxides. *Prog. Mater. Sci.* **2007**, *52*, 597–647.

(35) Pechini, M. P. Method of preparing lead and alkaline earth titanates and niobates and coating method using the same to form a capacitor. US patent number 3330697, 1967.

(36) Fitch, A. N. The high resolution powder diffraction beamline at the ESRF. *J. Res. Natl. Inst. Stand. Technol.* **2004**, *109*, 133–142.

(37) Rietveld, H. M. A Profile Refinement Method for Nuclear and Magnetic Structures. *J. Appl. Crystallogr.* **1969**, *2*, 65–71.

(38) Larson, A. C.; Von Dreele, R. B. *General Structural Analysis System (GSAS); Los Alamos National Laboratory Report LAUR 86-748*; 2004.

(39) Lobanov, N. N.; Alte da Veiga, L. *6th European Powder Diffraction Conference*, August 22–25, Hungary, Budapest, 1998; abstract P12–16.

(40) Thompson, P.; Cox, D. E.; Hastings, J. B. Rietveld refinements of Debye Scherrer synchrotron X-Ray data from Al$_2$O$_3$. *J. Appl. Crystallogr.* **1987**, *20*, 79–83.

(41) Qiu, X.; Thompson, J. W.; Billinge, S. L. J. PDFgetX2: A GUI driven program to obtain the pair distribution function from X-ray powder diffraction data. *J. Appl. Crystallogr.* **2004**, *37*, 678.

(42) Farrow, C. L.; Juhás, P.; Liu, J. W.; Bryndin, D.; Božin, E. S.; Bloch, J.; Proffen, T.; Billinge, S. J. L. PDFfit2 and PDFgui: computer programs for studying nanostructure in crystals. *J. Phys.: Condens. Matter* **2007**, *19*, 335219.

(43) Qiu, X.; Bozin, E. S.; Juhas, P.; Proffen, T.; Billinge, S. J. L. Reciprocal-space instrumental effects on the real-space neutron atomic pair distribution function. *J. Appl. Crystallogr.* **2004**, *37*, 110–116.

(44) Williamson, G. K.; Hall, W. H. X-ray line broadening from filed aluminium and wolfram. *Acta Metall.* **1953**, *1*, 22–31.

(45) Artini, C.; Pani, M.; Lausi, A.; Masini, R.; Costa, G. A. High Temperature Structural Study of Gd-Doped Ceria by Synchrotron X-ray Diffraction (673 K ≤ T ≤ 1073 K). *Inorg. Chem.* **2014**, *53*, 10140–10149.

(46) Adachi, G.-Y.; Imanaka, N. The Binary Rare Earth Oxides. *Chem. Rev.* **1998**, *98*, 1479–1514.

(47) Hirosaki, N.; Ogata, S.; Kocer, C. Ab initio calculation of the crystal structure of the lanthanide Ln$_2$O$_3$ sesquioxides. *J. Alloys Compd.* **2003**, *351*, 31–34.

(48) Checchia, S.; Scavini, M.; Allieta, M.; Brunelli, M.; Ferrero, C.; Coduri, M. Size and spatial correlation of defective domains in yttrium-doped CeO$_2$. *Powder Diff.* **2015**, *30*, S119–S126.

(49) Grover, V.; Tyagi, A. K. Phase relations, lattice thermal expansion in $CeO_2-Gd_2O_3$ system, and stabilization of cubic gadolinia. *Mater. Res. Bull.* **2004**, *39*, 859−866.

(50) Coduri, M.; Scavini, M.; Pani, M.; Carnasciali, M. M.; Klein, H.; Artini, C. From nano to microcrystals: effects of different synthetic pathways on the defect architecture in heavily Gd-doped ceria. *Phys. Chem. Chem. Phys.* **2017**, *19*, 11612−11630.

(51) Shannon, R. D. Revised Effective Ionic Radii and Systematic Studies of Interatomic Distances in Halides and Chalcogenides. *Acta Crystallogr., Sect. A: Cryst. Phys., Diffr., Theor. Gen. Crystallogr.* **1976**, *32*, 751−767.

(52) Scavini, M.; Coduri, M.; Allieta, M.; Mollica, L.; Brunelli, M.; Malavasi, L.; Lascialfari, A.; Ferrero, C. Unveiling the mesoscopic disorder induced by Al-doping in $SmBa_2Cu_{3-x}Al_xO_{6+\delta}$ superconductors by mean of the reciprocal and real space analysis of Synchrotron Radiation XRPD data. *J. Phys. Chem. C* **2010**, *114*, 19509−19520.

(53) Argyriou, D. N. Measurement of the static disorder contribution to the temperature factor in cubic stabilized ZrO_2. *J. Appl. Crystallogr.* **1994**, *27*, 155−158.

(54) Hammer, M. S.; Deibel, C.; Rauh, D.; Lorrmann, V.; Dyakonov, V. Effect of doping− and field−induced charge carrier density on the electron transport in nanocrystalline ZnO. *Nanotechnology* **2008**, *19*, 485701.

(55) Ohyanagi, M.; Yamamoto, T.; Kitaura, H.; Kodera, Y.; Ishii, T.; Munir, Z. A. Consolidation of nanostructured SiC with disorder− order transformation. *Scr. Mater.* **2004**, *50*, 111−114.

(56) Allieta, M.; Brunelli, M.; Coduri, M.; Scavini, M.; Ferrero, C. Differential Pair Distribution Function applied to $Ce_{1-x}Gd_xO_{2-x/2}$ system. *Zeitschrift für Kristallographie Proceedings* **2011**, *1*, 15−20.

(57) Nakamura, A. New defect-crystal-chemical approach to non-Vegardianity and complex defect structure of fluorite-based $MO_2-LnO_{1.5}$ solid solutions (M^{4+}=Ce, Th; Ln^{3+}=lanthanide) part I: Model description and lattice-parameter data analysis. *Solid State Ionics* **2010**, *181*, 1631−1653.

(58) Gschneidner, K. A.; Eyring, L. *Handbook on the Physics and Chemistry of Rare Earths*. North-Holland Publishing Company, 1979; Chapter 27.

(59) Coduri, M.; Scavini, M.; Allieta, M.; Brunelli, M.; Ferrero, C. Local disorder in yttrium doped ceria ($Ce_{1-x}Y_xO_{2-x/2}$) probed by joint X-ray and Neutron Powder Diffraction. *J. Phys.: Conf. Ser.* **2012**, *340*, 012056.

(60) Leoni, M.; Confente, T.; Scardi, P. PM2K: A flexible program implementing Whole Powder Pattern Modelling. *Z. Kristallogr. Suppl.* **2006**, *23*, 249−254.

(61) Chavan, S. V.; Tyagi, A. K. Phase relations and lattice thermal expansion studies in the $Ce_{0.50}RE_{0.50}O_{1.75}$ (RE = rare-earths). *Mater. Sci. Eng., A* **2005**, *404*, 57−63.

(62) Yoshida, H.; Deguchi, H.; Miura, K.; Horiuchi, M.; Inagaki, T. Investigation of the relationship between the ionic conductivity and the local structures of singly and doubly doped ceria compounds using EXAFS measurement. *Solid State Ionics* **2001**, *140*, 191−199.

(63) Andersson, D. A.; Simak, S. I.; Skorodumova, N. V.; Abrikosov, I. A.; Johansson, B. Optimization of ionic conductivity in doped ceria. *Proc. Natl. Acad. Sci. U. S. A.* **2006**, *103*, 3518−3521.

(64) Wagemaker, M.; Borghols, W. J. H.; Mulder, F. M. Large Impact of Particle Size on Insertion Reactions. A Case for Anatase Li_xTiO_2. *J. Am. Chem. Soc.* **2007**, *129* (14), 4323−4327.

(65) Artini, C.; Costa, G. A.; Pani, M.; Lausi, A.; Plaisier, J. Structural characterization of the CeO_2/Gd_2O3 mixed system by synchrotron X-ray diffraction. *J. Solid State Chem.* **2012**, *190*, 24−28.